Seasonal changes of the baroclinic wave activity in the northern hemisphere of Mars simulated with a GCM

Takeshi Kuroda,[1] Alexander S. Medvedev,[1] Paul Hartogh,[1] and Masaaki Takahashi[2]

[1] Seasonal changes in baroclinic wave activity during northern autumns ($L_s = 195–225°$) and winters ($L_s = 280–300°$) are studied with a Martian general circulation model. For the weak dust load, the simulated $s = 2$ harmonic with 3.1 sols period dominates near the surface, while $s = 1$ (5.5 sols period) is more prominent at higher altitudes during autumns. In winters, the $s = 1$ wave has stronger amplitudes and a deep (up to 0.1 mb) vertical structure. These simulations are consistent with observations from MGS. We provide a simple explanation for the planetary wave changes in terms of seasonal variations of the background zonal mean fields. In particular, the observed and simulated significant reduction of the baroclinic wave activity during strong solstitial season dust storms occurs due to the stabilization of the jet stream with respect to baroclinic disturbances, and due to the associated weakening of the wave excitation. **Citation:** Kuroda, T., A. S. Medvedev, P. Hartogh, and M. Takahashi (2007), Seasonal changes of the baroclinic wave activity in the northern hemisphere of Mars simulated with a GCM, *Geophys. Res. Lett.*, *34*, L09203, doi:10.1029/2006GL028816.

1. Introduction

[2] Regularly occurring traveling planetary waves with periods from 2 to 10 sols (Martian days) were observed by Mars Viking Landers [*Barnes*, 1980, 1981] and Mars Global Surveyor (MGS) [*Wilson et al.*, 2002; *Banfield et al.*, 2004; *Hinson*, 2006] in the northern hemisphere of Mars from autumn to spring. They are believed to be generated by the baroclinic instability of the mean flow. The spectrum of traveling waves consists of various well-defined harmonics with certain dominating modes at each time and the transition between them [*Hinson*, 2006]. The most prominent modes are the eastward moving waves with the zonal wave numbers $s = 1$, 2, and 3 with the corresponding periods of ~ 6 sols, 3 to 4 sols, and ~ 2 sols. The MGS Thermal Emission Spectrometer (TES) data show that during $L_s = 195–225°$ ("northern autumn"), the harmonic $s = 1$ and ~ 6 sols period (hereafter denoted as "~ 6 sols, $s = 1$") and the (~ 3 sols, $s = 2$) wave have about the same amplitudes near the surface. The (~ 6 sols, $s = 1$) harmonic dominates at higher altitudes [*Banfield et al.*, 2004]. The oscillations during the "northern winter" ($L_s = 280–300°$) are composed mostly of the (~ 6.5 sols, $s = 1$) mode. The amplitude of this wave is stronger than that of its counterpart with a slightly shorter period (~ 6 sols, $s = 1$) in autumn, especially above the surface [*Wilson et al.*, 2002]. Near the surface, the baroclinic waves do not penetrate poleward of $\sim 70°$N in winter, but they can extend up to $\sim 80°$N in autumn [*Wilson et al.*, 2002; *Banfield et al.*, 2004; *Hinson*, 2006]. Harmonics (2 to 3 sols, $s = 3$) are observed by MGS in both autumn and winter [*Banfield et al.*, 2004; *Hinson*, 2006].

[3] Occurrences of dust storms seriously modify traveling wave characteristics in winter. The spectral analysis of the Viking Lander 2 data showed that the planet-encircling dust storm observed after the winter solstice in 1977 caused a significant reduction of the wave activity accompanied by the increase of the zonal wave number of the dominant harmonic [*Barnes*, 1980, 1981].

[4] Baroclinic waves and their variability have been studied using Martian general circulation models (MGCM). MGCMs reproduced the $s = 1$ to 3 harmonics for the low dust conditions (opacity of 0.2–0.3 in visible wavelengths) [*Barnes et al.*, 1993; *Collins et al.*, 1996, *Wilson et al.*, 2002]. In the experiments with larger dust opacities corresponding to planet-encircling dust storms, *Barnes et al.* [1993] could not capture the significant reduction of the planetary wave activity. *Hourdin et al.* [1995] reported a weakening of transient surface pressure variations in the simulations with the LMD MGCM under strong dust conditions. Although not considered in detail, their result suggested a suppression of the baroclinic waves in their model with an increased dust load, especially after the winter solstice. Recently, *Basu et al.* [2006] presented seasonal variations of the amplitudes and periods of the dominant wave harmonics with $s = 1$ to 3 simulated with the GFDL MGCM near the surface.

[5] The seasonal behavior of baroclinic waves as well as the changes associated with an increased atmospheric dust load is examined here using a newly developed MGCM [*Kuroda et al.*, 2005]. It was recently realized that (~ 2 sols, $s = 3$) harmonics can play an important role in the Martian meteorology by initiating southward-moving flushing dust storms [*Wang et al.*, 2003, 2005; *Basu et al.*, 2006]. These "fast" waves have a shallow vertical structure and are usually confined to the lower atmospheric scale height. We focus on the first two harmonics $s = 1$ and 2, which can propagate upward and to affect the circulation in the upper atmosphere.

2. General Circulation Model Description

[6] The model used in this study was developed from the terrestrial CCSR/NIES (Center for Climate System Research/National Institute of Environmental Studies, Japan) GCM [*Kuroda et al.*, 2005; *Kuroda*, 2006]. The model employs a spectral solver with T21 horizontal resolution ($\sim 5.6°$ in both longitude and latitude) in the runs to be reported on. The vertical resolution is 30 σ-levels with the top at about 80 km. Realistic topography, albedo, and

[1]Max-Planck-Institute for Solar System Research, Katlenburg-Lindau, Germany.
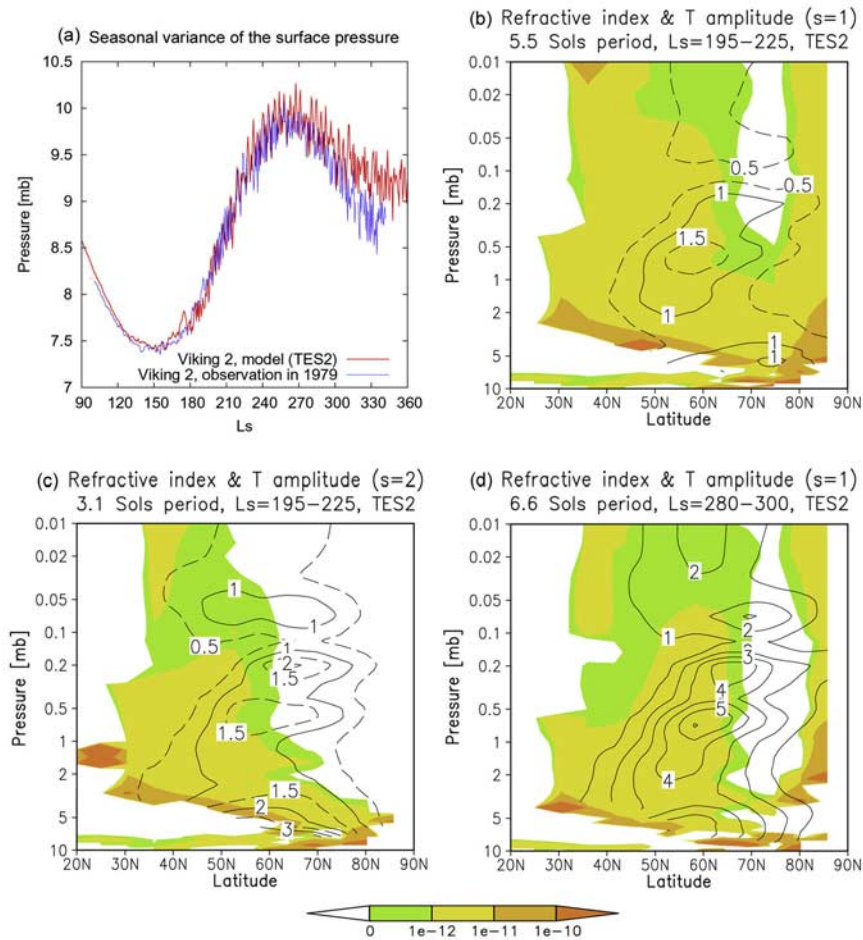[2]Center for Climate System Research, University of Tokyo, Kashiwa, Japan.

Figure 1. Baroclinic wave properties simulated with the "weak dust" scenario: (a) simulated daily-averaged surface pressure variations at 47°N, 225°W (red) and those observed by Viking Lander 2 in 1979 (blue) (plotted data were taken from S. W. Lee (Viking Lander meteorology and atmospheric opacity data set, NASA Planet. Data Syst., available at http://atmos.nmsu.edu/PDS/data/vl_1001/, 1995)); (b) height-latitude cross-section of squared refractive index (m^{-2}, shades) and the temperature amplitude (contours) for the (5.5 sols, $s = 1$) wave in "autumn"; (c) same as Figure 1b except for the (3.1 sols, $s = 2$) harmonic in "autumn" ($L_s = 195°–225°$); and (d) same as Figure 1b except for the (6.6 sols, $s = 1$) wave in "winter" ($L_s = 280°–300°$).

thermal inertia distributions at the Mars surface are included. CO_2 condensation and sublimation processes are accounted for as in *Forget et al.* [1998]. The model computes heating and cooling rates due to the absorption and emission by CO_2 infrared bands, and by the atmospheric dust in solar and infrared wavelengths between 0.2 and 200 μm, using the radiative scheme MSTRN-X with 19 representative wavelength bands: 9 in the visible and 10 in the infrared spectral range [*Nakajima et al.*, 2000; *Sekiguchi*, 2004]. The spatial and temporal dust distributions are prescribed to fit the measurements. In particular, the "weak dust" scenario, TES2, corresponds to the MGS-TES Year 2 observations, and the "strong dust" scenario, VIK1, follows the Viking Year 1 data. These scenarios are described by *Kuroda et al.* [2005] in full detail.

3. Seasonal Changes of the Simulated Traveling Waves

[7] Figure 1a compares the simulated annual cycle of the daily-mean surface pressure at 47°N, 225°W with Viking

Lander 2 measurements in 1979 (S. W. Lee, Viking Lander meteorology and atmospheric opacity data set, NASA Planet. Data Syst., available at http://atmos.nmsu.edu/PDS/data/vl_1001/, 1995) for the "weak dust" scenario (the global mean visible dust opacity is ~0.2 between $L_s = 195°–300°$). It shows a quantitative agreement between the model and observations in both the magnitude of the pressure perturbations and the time of their occurrence, especially in the summer and autumn. Further, we shall consider two time intervals: $L_s = 195°–225°$ (the "autumn") and $L_s = 280°–300°$ (the "winter"). These intervals were chosen as a compromise between several somewhat contradicting requirements. For example, the intervals must be long enough to resolve long-period harmonics and short enough to capture their observed correlation times [*Banfield et al.*, 2004; *Hinson*, 2006]. They should be separated in time such that the same wave trains do not contribute to both seasonal spectra, and must be centered near the areocentric longitude L_s corresponding to the season. Spectral analysis for the "autumn" yields three dominant harmonics: (5.5 sols, $s = 1$), (3.1 sols, $s = 2$), and (5 sols, $s = 2$).
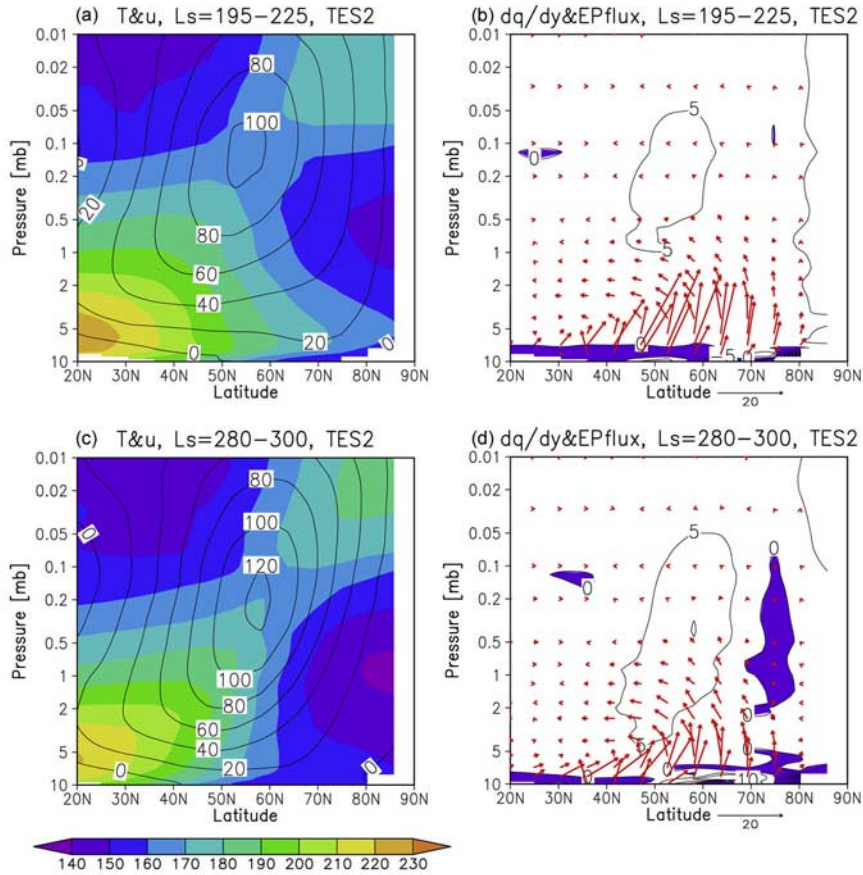
Figure 2. Zonal-mean atmospheric fields simulated with the "weak dust" scenario: (a) Temperature (K, shades) and zonal wind (m s^{-1}, contours); (b) Eliassen-Palm fluxes due to transient eddies (red arrows) and the meridional gradient of the potential vorticity $\bar{q}_y$ multiplied by the radius of Mars [$\times 10^{-4}$ s^{-1}] averaged for the "autumn" ($L_s = 195°-225°$). Shaded are the negative values; and (c and d) same as Figures 2a and 2b, respectively, except for the "winter" ($L_s = 280°-300°$).

The periods of the first two waves are consistent with the corresponding analysis of the Viking Lander 2 data [*Barnes*, 1981], while the third harmonic was not detected. Note that the (5 sols, $s = 2$) wave strongly decreases with height in our simulations. The height-latitude cross-sections of the amplitudes of temperature for waves (5.5 sols, $s = 1$) and (3.1 sols, $s = 2$) in "autumn" are plotted in Figures 1b and 1c, respectively. The squared refractive index for the corresponding components [e.g., *Andrews et al.*, 1987]

$$n_s^2 = \frac{\bar{q}_y}{\bar{u} - c} - \frac{s^2}{a^2 \cos^2 \phi} - \frac{f^2}{4N^2 H^2}, \qquad (1)$$

where $\bar{q}_y$ is the mean potential vorticity gradient, is superimposed in Figures 1b and 1c. In (1),

$$\bar{q}_y = \beta - f^2 \rho^{-1} \left(\rho N^{-2} \bar{u}_z \right)_z - \bar{u}_{yy}, \qquad (2)$$

$\bar{u}$ is the zonal-mean zonal wind velocity, c is the phase speed of the wave component, a is the radius of the planet, ϕ is the latitude, f is the Coriolis parameter, N is the Brunt-Väisälä frequency, H is the scale height, $\beta = df/dy$ and ρ is the atmospheric density. Figures 1b and 1c show that the shaded area with $n_s^2 > 0$, which denotes regions of free vertical and meridional wave propagation, is broader for the (5.5 sols, $s = 1$) harmonic. This favors the upward propagation of the

$s = 1$ wave compared to the $s = 2$ one. Note that the amplitudes of the (3.1 sols, $s = 2$) wave at 0.5 mb are weaker than the amplitudes near the surface, whereas the (5.5 sols, $s = 1$) has comparable magnitudes near the surface and higher. This behavior is consistent with the MGS-TES data [*Banfield et al.*, 2004].

[8] In "winter," the simulated oscillations are dominated by the (6.6 sols, $s = 1$) harmonic both near the surface and higher. The other (weaker) waves present in the simulations are (3 to 3.5 sols, $s = 2$) and (2 to 2.3 sols, $s = 3$). Figure 1d shows the amplitude and the squared refractive index for the wave $s = 1$. It is seen that the amplitude of the dominant harmonic is much larger compared to its counterpart (5.5 sols, $s = 1$) in "autumn". The distribution of n_s^2 prevents wave propagation northward of $\sim 70°$ N at all heights rather than only above 0.5 mb in autumn. Since temperature perturbations are proportional to the vertical gradient of the perturbations of the geopotential, the areas of a strong vertical decay of the wave geopotential coincide with areas of large amplitudes of the wave temperature. It is seen from Figure 1d that the maximum of temperature fluctuations associated with the harmonic (5.5 sols, $s = 1$) occurs along the line $n_s^2 = 0$. These features agree well with the MGS-TES and MGS radio occultation data [*Wilson et al.*, 2002; *Banfield et al.*, 2004; *Hinson*, 2006], and were reproduced with MGCM [*Wilson et al.*, 2002].
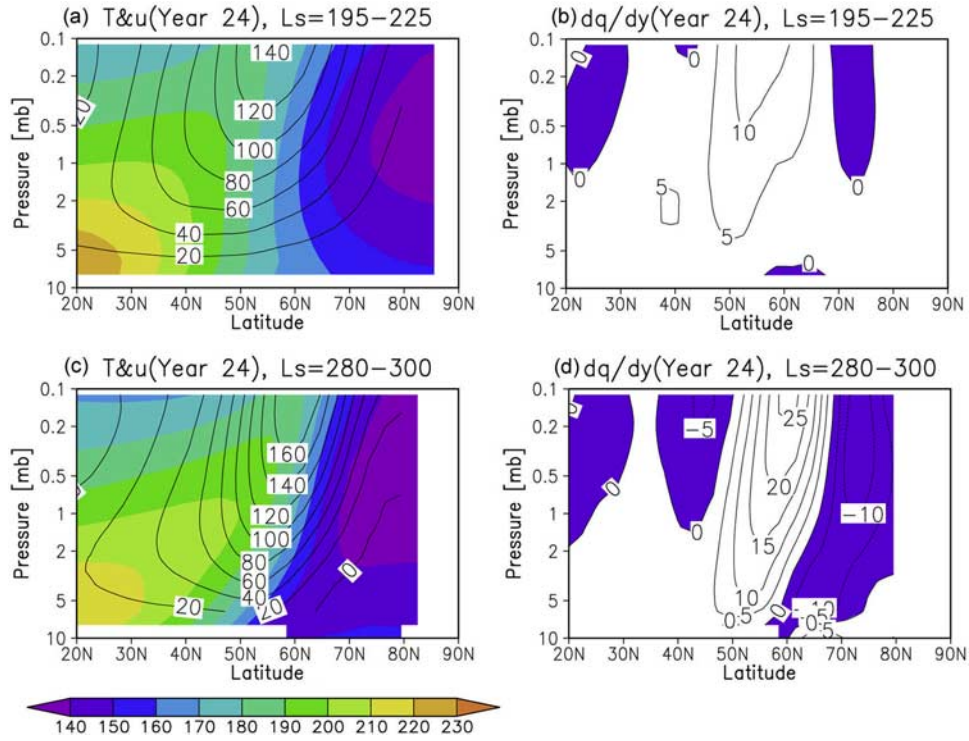
Figure 3. Same as in Figure 2, except calculated from the MGS-TES nadir data for Mars Year 24.

[9] To explain the seasonal changes in the properties of baroclinic waves, we plotted the simulated zonal mean wind and temperature for "autumn" and "winter" in Figure 2. It is seen that the meridional temperature gradient in the northern midlatitudes increases in the "winter". As the result, the westerly jet stream becomes stronger causing larger vertical wind shear below ~1 mb. These changes in the zonal circulation affect the traveling wave excitation. According to the linear estimations of instability growth rates [*Branscome*, 1983], larger vertical wind shears, $\bar{u}_z$, shift the most unstable harmonic in the flow to smaller wave numbers, k_{max}, and increase its baroclinic growth rate, σ_{max}:

$$\sigma_{max} \propto \frac{f\bar{u}_z}{N}, \quad k_{max} \propto \frac{(1+\gamma)f}{NH}, \quad (3)$$

where

$$\gamma = \frac{\beta N^2 H}{f^2 \bar{u}_z}. \quad (4)$$

In other words, the expansion of the CO_2 polar cap in winter stabilizes the low-level polar vortex with respect to shorter wave disturbances and increases the longer wave instability. This is qualitatively consistent with the shift of the dominant wave number from $s = 2$ in "autumn" to 1 in "winter". Note that the employed *Branscome* [1983] analysis is an approximation in the 'short-wave' limit. It is fully applicable here for harmonics with $s \geq 2$ with all meridional shapes, and for harmonics $s = 1$ with the meridional wave numbers $l \geq 2$.

[10] Now turn to the spatial distributions of the baroclinic waves. The potential vorticity gradient, $\bar{q}_y$, plotted in Figures 2b and 2d contains a useful information on the wave generation. A change of sign of $\bar{q}_y$ in the domain represents a necessary condition for the instability, and indicates potential areas of wave excitation. Comparison of $\bar{q}_y$ distributions shows that the flow near the surface is likely a source of baroclinic and/or barotropic traveling waves in both seasons. In addition, the potential vorticity gradient becomes negative in the upper part of the atmosphere (between 0.1 and 2 mb) at ~70°N in "winter" due to stronger $\bar{u}_{zz}$ and/or $\bar{u}_{yy}$ (see equation (2)), while there is no corresponding area with $\bar{q}_y < 0$ during the "autumn" (Figures 2b and 2d). Therefore, this area may potentially be a source of waves in winter. At the same time, as follows from (1), larger negative values of $\bar{q}_y$ at ~70°N prevent the waves from penetrating northward. To explore the relative importance of low-level and upper-level wave generation, we plotted the Eliassen-Palm (EP) fluxes associated with the transient eddies in Figures 2b and 2d. It is seen that the magnitude of EP fluxes near the surface are almost twice as larger in the "autumn" than that in the "winter", however the EP fluxes decrease strongly with height. EP fluxes near the area of negative $\bar{q}_y$ above 2 mb over ~70°N are about 30% stronger in winter suggesting that the instability in these upper layers contributes to some degree to traveling wave generation. Thus, our analysis shows that the dominant transient waves are generated largely near the surface during both the "autumn" and "winter" with stronger excitation in autumn. In addition, the instability in the upper (1 to 0.2 mb) layers and favorable propagation conditions can explain stronger baroclinic wave activity in winter.

[11] To compare the simulations with observations, we present similar plots computed from the MGS-TES nadir data for Mars Year 24 for the time without global dust storms. The zonal mean wind (Figures 3a and 3c) was calculated from the MGS-TES temperature using the thermal wind relation [e.g., *Andrews et al.*, 1987] and
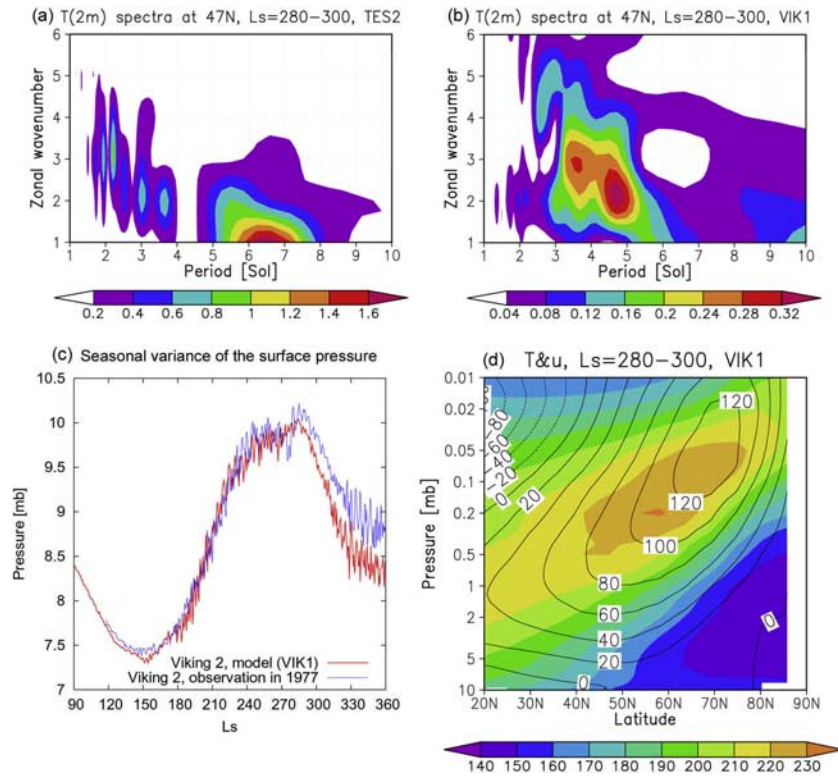
Figure 4. Baroclinic wave properties simulated in the model for the "winter" ($L_s = 280°-300°$): (a) spectral decomposition of 2 m-height temperature variations at 47°N for the "weak dust" scenario; (b) same as Figure 4a except for the "strong dust" scenario; (c) simulated daily-averaged surface pressure variations at 47°N, 225°W for the "strong dust" scenario (red) and those observed by Viking Lander 2 in 1977 (blue); and (d) same as in Figure 2c except for the "strong dust" scenario.

assuming $\bar{u} = 0$ at ~7.8 mb. Note that the potential vorticity gradient calculated from the estimated velocities might contain considerable errors. Therefore, we consider these results as only indicative of the tendencies in the change of values, but do not rely on the values themselves. Both the model and observation (Figures 2 and 3) agree in that the vertical wind shear in midlatitudes increases in the "winter" compared to the "autumn", and the area with negative $\bar{q}_y$ at ~70°N becomes larger. The stronger baroclinic instability of the flow in "winter" possibly generates the $s = 1$ mode throughout the atmosphere, but the mean zonal wind distribution traps it southward of 70°N.

4. Changes Induced by a Planet-Encircling Dust Storm

[12] Strong dust storms in the Martian atmosphere significantly affect the characteristics of the traveling waves. Figures 4a and 4b shows the spectral decompositions of the 2-meter height temperature oscillations at 47°N for the "winter" simulated using the "weak" and "strong" dust scenarios. In the latter, the dust opacity was prescribed to imitate the occurrence of the planet-encircling storm in 1977. This storm started at $L_s \sim 280°$ and lasted for 30–40 days. Note that the global mean visible dust opacity in "winter" for this scenario reaches ~4.2. As seen in Figures 4a and 4b, the dominant waves near the surface have larger wave numbers and significantly (about an order of magnitude) smaller amplitudes during the dust storm.

This is qualitatively consistent with the results of the spectral analysis of the Viking Lander 2 data [*Barnes*, 1980]. The time series of the observed and simulated surface pressure (Figure 4c) show a significant reduction of the oscillations associated with traveling waves after the onset of the storm at $L_s \sim 280°$. These changes in baroclinic waves are directly related to the changes in the mean circulation caused by dust storms. Figure 4d presents the simulated zonal mean temperature and zonal wind for the "strong dust" scenario. The temperature above ~1 mb at 50–80°N rises by up to ~60 K, which is comparable to that observed by Viking spacecraft [*Martin and Kieffer*, 1979]. This strong heating was not reproduced in MGCM experiments of *Barnes et al.* [1993], which apparently resulted in the failure to simulate the reduction of the oscillations. The low-level vertical wind shear above the midlatitudes decreases as the result of the meridional temperature gradient flattening (see Figure 2c). In particular, $\bar{u}_z$ is less than 0.001 s^{-1} near the surface compared to ~0.006 s^{-1} under the "weak dust" scenario. The weaker wind shear not only stabilizes the flow with respect to the baroclinic perturbations (σ_{max} decreases six times, as follows from equation (3)), but also increases the wave number of the most unstable mode, k_{max}, by a factor 2.67, as follows from (3) and (4). Therefore, the reduction of baroclinic wave activity during dust storms is caused by the weaker wave generation in the lower part of the atmosphere. At higher altitudes, our simulations still show weak oscillations with amplitudes of about 1.5 K near 0.4 mb. They are likely

associated with in-situ generated baroclinic eddies since the analysis of EP fluxes shows virtually no signal of waves penetrated from below [*Kuroda*, 2006].

5.   Summary and Conclusions

[13]   Baroclinic waves with zonal wave numbers 1 and 2 observed during autumns and winters in the northern hemisphere of Mars were studied with a newly developed MGCM [*Kuroda et al.*, 2005; *Kuroda*, 2006]. The simulations reproduced the main features of the traveling wave disturbances as well as their observed seasonal changes. These variations are closely related to changes in the zonal mean wind and temperature structure and the associated baroclinic instability. During a "weak dust" autumn (L_s = 195°–225°), the $s = 2$ harmonic with 3.1 sols period is dominant near the surface. The vertical distribution of the amplitudes of the $s = 1$ (5.5 sols period) and $s = 2$ harmonics are qualitatively consistent with the MGS-TES observations. At higher altitudes, the $s = 1$ component tends to be relatively large due to favorable vertical propagation conditions, as the refractive index distribution indicates. Both waves are originated mostly near the surface.

[14]   During a "weak dust" winter, the $s = 1$ wave with 6.6 sols period dominates both near the surface and up to 0.1 mb. The shift of the dominant wave number from $s = 2$ in autumn to $s = 1$ in winter is consistent with the linear baroclinic stability analysis: the stronger vertical wind shear in winter increases the instability growth rates and shifts the most unstable mode to longer wavelengths. These seasonal changes of the wave properties are qualitatively consistent with the MGS observations. Our simulations suggest that the flow near the surface is a strong source of traveling waves during both autumn and winter. In winter, the polar night jet becomes more unstable up to 0.1 mb, and, possibly, can excite waves along with the low-level flow. In-situ generation and the propagation from below explain the deep vertical structure and significantly stronger amplitudes of the dominant wave mode in winter. With the expansion of the CO_2 ice cap during winters, the near surface baroclinic wave activity shifts southward, accordingly. The potential vorticity gradient in the upper layers (up 0.1 mb) turns negative near ~70°N, thus modifying the refractive index and preventing the waves from propagating northward. This explains why wave disturbances were not detected in high latitudes in winters.

[15]   The model reproduces a significant reduction of the baroclinic wave activity near the surface during strong planet-encircling dust storms in winter. The spectral analysis show that harmonics with higher wave numbers $s = 2$ to 4 become dominant, instead of the $s = 1$ wave in the "weak dust" simulation, which is qualitatively consistent with the Viking Lander observations. The dust storm enhances the mean meridional circulation and increases the temperature in high latitudes. The decreased meridional temperature gradient and weaker wind shear near the surface in midlat-itudes stabilize the flow, and, thus, reduce the baroclinic wave generation and increase the dominant wave numbers.

References

Andrews, D. G., J. R. Holton, and C. B. Leovy (1987), *Middle Atmosphere Dynamics*, *Int. Geophys. Ser.*, vol. 40, edited by R. Dmowska and J. R. Holton, 489 pp., Academic, Orlando, Fla.

Banfield, D., B. J. Conrath, P. J. Gierasch, R. J. Wilson, and M. D. Smith (2004), Traveling waves in the Martian atmosphere from MGS TES nadir data, *Icarus*, *170*, 365–403.

Barnes, J. R. (1980), Time spectral analysis of midlatitude disturbances in the Martian Atmosphere, *J. Atmos. Sci.*, *37*, 2002–2015.

Barnes, J. R. (1981), Midlatitude disturbances in the Martian atmosphere: A second Mars year, *J. Atmos. Sci.*, *38*, 225–234.

Barnes, J. R., J. B. Pollack, R. M. Haberle, R. W. Zurek, C. B. Leovy, H. Lee, and J. Schaeffer (1993), Mars atmospheric dynamics as simulated by the NASA/Ames general circulation model: 2. Transient baroclinic eddies, *J. Geophys. Res.*, *98*, 3125–3148.

Basu, S., J. Wilson, M. Richardson, and A. Ingersoll (2006), Simulation of spontaneous and variable global dust storms with the GFDL Mars GCM, *J. Geophys. Res.*, *111*, E09004, doi:10.1029/2005JE002660.

Branscome, L. E. (1983), The Charney baroclinic stability problem: Approximate solutions and model structures, *J. Atmos. Sci.*, *40*, 1393–1409.

Collins, M., S. R. Lewis, P. L. Read, and F. Hourdin (1996), Baroclinic wave transitions in the Martian atmosphere, *Icarus*, *120*, 344–357.

Forget, F., F. Hourdin, and O. Talagrand (1998), CO_2 Snowfall on Mars: Simulation with a General Circulation Model, *Icarus*, *131*, 302–316.

Hinson, D. P. (2006), Radio occultation measurements of transient eddies in the northern hemisphere of Mars, *J. Geophys. Res.*, *111*, E05002, doi:10.1029/2005JE002612.

Hourdin, F., F. Forget, and O. Talagrand (1995), The sensitivity of the Martian surface pressure and atmospheric mass budget to various parameters: A comparison between numerial simulations and Viking observations, *J. Geophys. Res.*, *100*, 5501–5523.

Kuroda, T. (2006), Study of the effects of dust in the Martian meteorology using a general circulation model, Ph.D. thesis, 132 pp., Univ. of Tokyo, Tokyo, 30 Nov.

Kuroda, T., N. Hashimoto, D. Sakai, and M. Takahashi (2005), Simulation of the Martian atmosphere using a CCSR/NIES AGCM, *J. Meteorol. Soc. Jpn.*, *83*, 1–19.

Martin, T. Z., and H. H. Kieffer (1979), Thermal infrared properties of the Martian atmosphere: 2. The 15-mm band measurements, *J. Geophys. Res.*, *84*, 2843–2852.

Nakajima, T., M. Tsukamoto, Y. Tsushima, A. Numaguti, and T. Kimura (2000), Modeling of the radiative process in an atmospheric general circulation model, *Appl. Opt.*, *39*, 4869–4878.

Sekiguchi, M. (2004), A study on evaluation of the radiative flux and its computational optimization in the gaseous absorbing atmosphere, Ph.D. thesis, 121 pp., Univ. of Tokyo, Tokyo, 25 Mar.

Wang, H., M. I. Richardson, R. J. Wilson, A. P. Ingersoll, A. D. Toigo, and R. W. Zurek (2003), Cyclones, tides, and the origin of cross-equatorial dust storms on Mars, *Geophys. Res. Lett.*, *30*(9), 1488, doi:10.1029/2002GL016828.

Wang, H., R. W. Zurek, and M. I. Richardson (2005), Relationship between frontal dust storms and transient eddy activity in the northern hemisphere of Mars as observed by Mars Global Surveyor, *J. Geophys. Res.*, *110*, E07005, doi:10.1029/2005JE002423.

Wilson, R. J., D. Banfield, B. J. Conrath, and M. D. Smith (2002), Traveling waves in the northern hemisphere of Mars, *Geophys. Res. Lett.*, *29*(14), 1684, doi:10.1029/2002GL014866.

––––––––––––––––

P. Hartogh, T. Kuroda, and A. S. Medvedev, Max-Planck-Institute for Solar System Research, Max-Planck-Str. 2, Katlenburg-Lindau D-37191, Germany. (kuroda@mps.mpg.de)

M. Takahashi, Center for Climate System Research, University of Tokyo, Kashiwa 277-8568, Japan.